1	TITLE PAGE		
2	Manuscript for submission to PNAS, Research Report		
3			
4	Classification: Physical Sciences (Earth, Atmospheric, and Planetary Sciences)		
5			
6	Title: Resolving seasonal rainfall changes in the Middle East during the last interglacial period		
7	Short title: Middle East rainfall seasonality at last interglacial		
8			
9	Authors: Ian J. Orlandı,*, Feng He2, Miryam Bar-Matthews3, Guangshan Chen1, Avner		
10	Ayalon3, John E. Kutzbach2		
11			
12	Affiliations:		
13 14 15 16 17 18	 Department of Geoscience, University of Wisconsin-Madison, 1215 W. Dayton St., Madison, WI, 53706, USA. Center for Climatic Research, Nelson Institute for Environmental Studies, University of Wisconsin-Madison, 1225 W. Dayton St., Madison, WI, 53706, USA. Geological Survey of Israel, 30 Malkei Israel St. Jerusalem, 95501, Israel. * Corresponding author: (608) 262-8960, orland@wisc.edu, ORCID: 0000-0002-4853-4111 		
20	Keywords: paleoclimate, seasonal-resolution, oxygen isotopes, data-model comparison		
21			

Abstract:

Paleorainfall proxy records from the Middle East have revealed remarkable patterns of variability since the penultimate glacial period (140 ka), but the seasonality of this signal has been unresolvable. Here, seasonal-resolution oxygen isotope data from Soreq Cave speleothems suggest that summer monsoon rainfall periodically reaches as for north as Israel – far removed from the modern monsoon – at times (~125, 105 ka) that overlap with evidence for some of the earliest modern human migrations out of Africa. These seasonal proxy data are corroborated by seasonal-resolution model output of the amount and oxygen-isotope ratio of rainfall from an isotope-enabled climate model. In contrast to the modern regional climate where rainfall is delivered predominantly in winter months along westerly storm tracks, the model suggests that during extreme peaks of summer insolation – as occurs during the last interglacial (e.g. 125, 105 ka) – regional rainfall increases due to both wetter winters and the incursion of summer monsoons. This interpretation brings clarity to regional paleoproxy records and provides important environmental context along one potential pathway of early modern human migration.

Significance Statement:

The Middle East was a gateway for early human migration out of Africa, and it is likely that the region's climate played an important role in this anthropogenic transition. This study is motivated by conflicting interpretations of rainfall seasonality from regional paleoenvironmental records. Specifically, we address whether summer monsoon rainfall may have expanded northward into the Middle East in the past. Today, the region has dry summers and relatively wet winters; the northern limit of the modern monsoon is far to the south. Here we combine climate modeling with seasonal-resolution geochemical analysis of cave carbonates from Israel and find

evidence for summer monsoon rainfall during recurrent intervals of the last interglacial period, which overlaps with archeological indicators of human migration.

/body

Introduction:

The oxygen isotope (δ_{18} O) record from Soreq Cave (Israel; Fig. 1) carbonate formations (speleothems) is a remarkable paleoclimate archive from a region of critical importance to understanding early migration of modern humans (1, 2), the development of civilization (3, 4), and Late Quaternary hydroclimate dynamics (5–7). The composite δ_{18} O record from Soreq speleothems (7, 8) spans the last 185 ka and has low-frequency variations of multiple permil that align with precession forcing of northern hemisphere insolation (Fig. 2A). The timing and magnitude of this variability has been hypothesized to reflect, in part, precessionally-forced monsoon flooding from North Africa that stratifies into a low- δ_{18} O freshwater lens atop the eastern Mediterranean (EM) Sea, inducing anoxic conditions and organic-rich sedimentation ("sapropels") at the EM seafloor when northern hemisphere summer insolation is high (9–12). The resulting decline of δ_{18} O values in EM surface water could then be transmitted to the cave site, where modern rainfall is sourced predominantly from the Mediterranean (5, 13).

Another potential contribution to the precession-paced pattern of δ_{18} O variability observed in Soreq is a northward expansion of summer monsoon circulation derived from the tropics during periods of high northern hemisphere insolation. At Soreq, the effect of Rayleigh fractionation (14) on distally-sourced monsoon rainfall would result in low- δ_{18} O summer rainfall that would decrease the annually-averaged δ_{18} O of rainfall above the cave. The connection between precession-paced insolation changes and summer monsoon dynamics (15) is well-

established in records of speleothem $\delta_{18}O$ from elsewhere in Asia (16, 17). Confoundingly, however, this pattern of δ_{18} O variability is also observed in speleothems from parts of Asia beyond the limits of the modern summer monsoon including Kesang Cave (Fig. 1) in northwestern China (18) and Soreq (6), which currently has a dry summer and receives most of its rainfall from westerly winter storm tracks. Some paleorainfall proxy records from the Middle East independently suggest that, indeed, the northern limit of summer monsoon rainfall delivery expands during precessional peaks in northern hemisphere (NH) insolation (e.g. 176, 125, 105, 85 ka) beyond its modern boundary to reach the Arabian Peninsula (19, 20) and the Levant (21, 22). In notable contrast, a modeling study that compares the regional climate dynamics in the EM between periods of maximum (125 ka) and minimum (115 ka) seasonal insolation gradient emphasizes that winter westerly storm tracks may deliver increased moisture to these regions when winter insolation is minimized (and summer insolation is maximized) (23). This emphasis on winter rainfall is invoked to explain increased moisture in the Levant at 125 ka (peak summer insolation) in a separate set of paleoclimate records (24, 25). Clearly, disentangling seasonal components of Middle Eastern paleoclimate records is critical for resolving the dynamics of monsoon variability as well as the interpretive differences in regional paleoclimate records. Together, these advances would elucidate a new, vital dimension of the environmental context for modern human migrations out of Africa.

68

69

70

71

72

73

74

75

76

77

78

79

80

81

82

83

84

85

86

87

88

89

90

Here, we take a two-pronged approach to evaluating the seasonal paleoclimate of the Middle East. First, rainfall simulations in an isotope-enabled climate model are used to examine the feasible geographic limits of summer monsoon rainfall and its isotopic signature. Given the well-established link between NH summer monsoon strength and summer insolation, modeling targeted the precession-forced summer insolation maximum at 125 ka – the highest summer

insolation peak during the last 185 ka of the Soreq speleothem record. Two comparative model runs were completed at sequential extremes of insolation seasonality (Fig. 2) – that is, Precession-High NH seasonality (PH; 125 ka) and Precession-Low NH seasonality (PL; 115 ka). The modeled amount and δ_{18} O of monthly rainfall was then extracted for the Levant region.

Next, we used an ion microprobe (or "SIMS") to test whether seasonal δ_{18} O signals recorded in Soreg speleothems at PH and PL are coherent with the model results for the Levant. The ion microprobe enables high-resolution (10-μm-diameter spots) in situ δ18O sampling of speleothem calcite, in contrast to conventional drill-sampling techniques that are limited to mmscale resolution. Combined with imaging of fluorescent growth banding in the Soreq speleothems, multiple ion microprobe analyses (n=2-9) were placed across individual annual growth bands to measure and compare patterns of seasonal δ18O variability through time. Given the sub-annual resolution of the ion microprobe $\delta_{18}O$ data, they must be treated in populations – much like weather observations – in order to interpret persistent changes in seasonal climate. This novel analytical approach was first developed in speleothem samples from Soreg Cave (26, 27; SI Appendix), and builds on an extended cave-monitoring program that has characterized Soreq hydrology (28) and demonstrated how seasonal climate signals are transmitted to the geochemistry of a modern Soreq speleothem (29). The current study leverages this extensive prior work at Soreq Cave to probe a crucial frontier in paleoclimate research: seasonal-resolution proxy-model comparison.

Results:

91

92

93

94

95

96

97

98

99

100

101

102

103

104

105

106

107

108

109

110

111

112

113

First, rainfall δ_{18} O is simulated by forcing an atmospheric model that incorporates δ_{18} O of rain and water vapor (isoCAM3) with boundary conditions derived from global climate

simulations of PH and PL in the coupled global climate model CCSM3 (see Materials and Methods). Rainfall amount and rainfall δ_{18} O output are averaged from the EM region using the same geographic boundaries as the prior modeling study (23) (Fig. 1) and binned into monthly intervals (Fig. 3).

114

115

116

117

118

119

120

121

122

123

124

125

126

127

128

129

130

131

132

133

134

135

136

Next, we compare the range of δ_{18} O variability (Δ_{18} O) observed within growth bands of two speleothems from Soreg Cave at time slices during precession-paced maxima (~125, 105 ka) and minimum (~115 ka) seasonal insolation gradients (Fig. 4). Earlier work describes the hydrology of the cave and demonstrates that Δ 18O in Soreg speleothems is a robust proxy of seasonal hydroclimate (26, 28, 29). In brief, seasonal variation of δ_{18} O is observed in modern Soreg rainwaters, dripwaters and speleothem growth bands with lowest δ_{18} O values during the winter wet season. The geochemistry and drip rates of modern Soreq dripwaters suggest that cave water is sourced from two reservoirs; a "baseline" reservoir with multi-decadal residence time supplies dripwater to the cave year-round, while a second reservoir delivers the more intense rains of the winter wet season (low- δ_{18} O) to the cave along more direct flowpaths (26, 28–30; SI Appendix). Hence, as previously corroborated in a modern Soreg speleothem, increased rainfall during a winter wet season correlates with lower δ_{18} O values of winter dripwaters relative to the baseline reservoir and results in a predictable increase in Δ_{18} O (28, 29). If, at 125 ka, low-δ18O monsoon rainfall were added to the summertime Levant hydroclimate, we hypothesize that Δ 18O within the growth bands of Soreq speleothems would have been smaller than at 115 ka because the additional summer rainfall would reduce the seasonal variability of dripwater δ_{18} O by decreasing the relative δ_{18} O of the baseline dripwater reservoir.

Model results indicate that monthly rainfall totals and rainfall $\delta_{18}O$ (Fig. 3 and SI Appendix) in the Levant are dramatically different during PH and PL, during both summer and

winter seasons. At PL boundary conditions, the CCSM3-isoCAM3 climate model pairing generates spatial and monthly rainfall patterns in the Levant that resemble the modern climate; the majority of annual rainfall occurs during a winter wet-season when δ18Orain is lowest. For PH boundary conditions, model output indicates increased winter rainfall but also significant northward expansion of the African and Asian summer monsoon belt (Fig. 1), such that there is significant rainfall during summer months (defined here as JAS, when PH rainfall δ_{18} O is distinctly lower than PL) in the Levant. Northward monsoon penetration in the Middle East is enhanced by westward expansion of the summertime "Persian Trough" low pressure system (31); this latitudinal extension of monsoon rainfall is independently observed in other models (32–34). In our model results for the region shown in Figure 1, there is a >4x increase in average JAS precipitation rate (0.15-0.67 mm/day; Fig. 3) in PH vs. PL and the new summer rainfall has a low δ_{18} O value similar to that of the modeled (and modern) winter precipitation. Notably, the modeled difference between precipitation and evaporation over land in the Levant is similar in both simulations and exhibits little seasonal change (SI Appendix). Hence, we predict that rainfall over the cave during PH has similarly low δ_{18} O_{rain} values during the wettest winter and summer months, which would result in lower intra-annual δ_{18} O variability (Δ_{18} O) in Soreg Cave speleothems.

137

138

139

140

141

142

143

144

145

146

147

148

149

150

151

152

153

154

155

156

157

158

159

Soreq Cave speleothem samples "SO-15" and "3-35" were previously dated with the U-Th geochronometer and analyzed for δ18O by conventional drilling methods (6, 8). For this study, imaging by confocal laser fluorescent microscopy (CLFM) revealed fluorescent banding in both samples akin to that observed in Soreq samples that grew during and after the last deglaciation (27). Earlier work finds repeated couplets of fluorescent ("bright") and non-fluorescent ("dark") bands in Soreq Cave speleothems to be annual markers with fluorescent

domains interpreted as wet seasons when organic matter in the overlying soil is flushed into the cave (29). Soreq speleothem sample SO-15 grew during both PH and PL and thus was ideal for comparing seasonal δ_{18} O gradients during both time periods. Sample 3-35 grew during PL and the preceding precession-paced NH insolation maximum ("~PH"; ~110-101 ka), which includes a brief interruption of sapropel event 4 (S4-gap, see Fig. 2) that coincides with a return of the Soreq δ_{18} O record to PL-like values (~108-105 ka; ref. 12). We make the analogous comparison in sample 3-35 of ~PH to combined observations from PL and the S4-gap interval in order to assess whether patterns of seasonal variability corroborate those observed in sample SO-15. Including both samples, a total of 601 SIMS analyses of δ_{18} O in 10- μ m spots were completed (SI Table S1). This total includes multiple spots (between 2-9 spots each) in ~50 individual bands in each sample.

In order to compare $\delta_{18}O$ variability within individual growth bands, we normalized the distance between SIMS analyses in the dark portion of sequential growth bands. Figure 4A schematically illustrates the placement, classification, and normalization of multiple SIMS analyses within a single fluorescent growth band. Figure 4B shows the $\delta_{18}O$ variability across two representative bands in sample SO-15 superimposed on the normalized distance scale and demonstrates how $\Delta_{18}O$ is calculated as the difference between the $\delta_{18}O$ of the bright fluorescent domain ("b"; winter wet season dripwater) and the dark domain ("d"; summer "baseline" dripwater) at the end of prior band. All normalized intra-band $\delta_{18}O$ data are plotted for each sample in SI Figure S1. A binned bootstrap randomization of the dataset from each sample (see Methods, SI Figure S1) shows that the observed intra-band $\delta_{18}O$ variability lies outside a randomized distribution with 95% confidence.

We highlight three key observations from the results. First, the patterns of intra-band

 δ_{18} O variability are not random (Fig. S1B). Second, the δ_{18} O value of bright domains is consistently the lowest measured within a band, regardless of time period (Fig. S1A). Third, the magnitude of intra-band δ_{18} O change (Δ_{18} O) differs between PH and PL (Figs. 2E and 4C). Mean Δ_{18} O in sample SO-15 is 0.36 during PH and increases to 0.57 during PL. In sample 3-35, mean Δ_{18} O is 0.52 during ~PH but is 0.73 for PL and S4-gap. The statistical significance of these changes in Δ_{18} O was then assessed as in prior work at Soreq (27).

The results of two statistical tests support the hypothesis that $\Delta_{18}O$ in Soreq speleothems during PH conditions would be different, and lower, with the addition of summer monsoon rainfall. First, a Kalmogorov-Smirnov (K-S) test indicates, for both speleothems, that populations of $\Delta_{18}O$ values measured during PH vs. PL conditions are from statistically distinct (p<0.05), normal distributions. Second, a two-sample t-test finds, again for both samples, that mean $\Delta_{18}O$ is smaller during PH than PL at the 95% confidence level (Fig. 4C). Further details are available in the SI Appendix.

Discussion:

To contextualize the observed decrease of seasonal $\delta_{18}O$ variability in Soreq speleothems at PH conditions, there are a number of climatic mechanisms with indirect and direct effects at Soreq Cave to consider. Here, we examine the expected impact of these mechanisms on the $\delta_{18}O$ of rainfall above Soreq Cave. First, an indirect effect on the source of Soreq rainfall: during PH, enhanced summer monsoon rainfall over northeast Africa increases Nile River outflow, causing EM surface water to freshen and weakening vertical mixing, which prompts sapropel formation in the EM (9, 10). The down-stream effect of this sequence on Soreq Cave – independent of changes in local climate – is to lower the $\delta_{18}O$ value of rainfall sourced from the EM. If the only

precipitation at Soreq during PH was winter rainfall sourced from the EM, then the $\delta_{18}O$ of annually-averaged rainfall at Soreq would be expected to decrease but the observed seasonal bias would not be imparted.

Likewise, the direct effects of predicted surface temperature and rainfall amount during PH vs. PL cannot explain the observed difference in Δ_{18} O. Rainfall monitoring and modern speleothem analysis at Soreq Cave shows that during the present-day winter-dominant rainfall regime, surface temperature positively correlates with rainfall δ_{18} O and rainfall amount negatively correlates with rainfall δ_{18} O (28, 29). Thus, neither the predicted warmer summers nor wetter winters of PH (23, 25) are, by themselves, consistent with smaller Δ_{18} O values.

Similarly, model results from this study combined with observations from the modern cave indicate that evaporation of surface and/or groundwater is unlikely to impart the observed Δ_{18} O signal. The modeled balance of evaporation and precipitation in the PH simulation is similar to PL (i.e. a modern analog) with little seasonal change. Since year-round sampling of modern dripwaters in Soreq Cave does not find an isotopic signature of evaporation (28), it is assumed that infiltration of rainwater at PH would also lack an isotopic signature of evaporation (SI Appendix). In sum, an additional climatic effect is needed to explain the decrease in Δ_{18} O values observed at PH.

The direct effect suggested by our rainfall-isotope-enabled modeling is the northward expansion during PH of low- δ_{18} O, summer monsoon rainfall that is most extensive along a corridor through the Middle East from the Indian Ocean to the shores of the EM (Figure 1). Relative to PL, when rainfall above Soreq Cave is delivered almost entirely by winter westerlies, the northward expansion of summer monsoon rainfall would act to both reduce annual rainfall δ_{18} O and decrease seasonal δ_{18} O variability recorded in speleothems. This mechanism offers a

self-consistent explanation for both the new seasonal-resolution speleothem geochemistry results and model realizations at PH and PL. The combination of our geochemical and model results provides a clear resolution to the intriguing ambiguity (35) of when and where monsoonal rainfall might impact the Mediterranean region.

229

230

231

232

233

234

235

236

237

238

239

240

241

242

243

244

245

246

247

248

249

250

251

Regional paleoclimate proxies have confounded this question with conflicting interpretations. One group of paleoclimate records dismiss the possibility of monsoonal expansion to the Mediterranean, but they either do not sample during PH or an equivalent insolation optimum (36, 37) or evaluate the Mediterranean basin as a whole (35) – our model suggests that the monsoon impact is confined to the EM. In contrast, another suite of regional paleoclimate proxies from pollen (38, 39) travertine (21), speleothem (19, 25, 40), relict lake deposits (41), leaf waxes (42), and Dead Sea sediment (22) records indicate increased moisture during PH along the Middle Eastern corridor between Indian Ocean and EM. Taken alone, however, these records cannot unambiguously assess the source or seasonality of additional moisture. To this end, earlier climate models provide support for the general northward expansion of monsoon rainfall during PH, but not far enough north to replicate either the increased summer moisture (43, 44) or decreased rainfall δ_{18} O values (45) interpreted from proxies. A more recent modelling study (23), however, does show increased winter and summer rainfall in the Middle East at PH, and emphasizes the importance of verifying this result with proxy observations.

Our interpretation of increased winter rainfall and an expanded range of the African-Asian summer monsoon to as far north as the Levant along a Middle Eastern corridor at ~125 and ~105 ka brings clarity to a rich collection of climate proxy records in the region.

Furthermore, this conclusion infers a remarkably dynamic latitudinal range of the summer

monsoon that is sensitive to the periodic variation of NH insolation. One implication that warrants further investigation of this type is on the duration, periodic timing, and geographic limits of habitable pathways for human migration out of Africa (46–48). Although it is still debated whether (49) or not (42) early human migrations out of Africa coincide with humid periods, we note that the age of the earliest human remains recently found in the Levant (2) may align with an analog of PH at ~176 ka (Figure 2A; refs 7, 50). Our conclusion supports the hypothesis that drastic changes in regional moisture availability that could enable such migration transpired on a recurring basis across the Pleistocene.

Materials and Methods:

Speleothem analysis

In preparation for ion microprobe analysis, sub-samples of Soreq Cave speleothems 3-35 and SO-15 (SI Figure S2) were ground flat for imaging using a water-lubricated, fixed-diamond lapping pad. In order to confirm the existence of fluorescent banding, samples were imaged by confocal laser fluorescent microscopy (CLFM) at the University of Wisconsin Optical Imaging Core on a Nikon A1Rs inverted-geometry microscope. A 488 nm excitation laser induced fluorescence that was imaged using 4x and 10x objective lenses to generate 1024x1024 pixel, tiff-formatted files (pixel dimension = $0.94\mu m$). Further description of this imaging method can be found in earlier studies (26, 51).

Speleothem sub-samples were then cut along an analytical transect, parallel to the direction of crystal growth. These transects were then sub-divided into 15mm-long pieces that were cast two-at-a-time (tip-to-tail), along with 3 grains of WiscSIMS calcite standard UWC-3 (12.49‰ VSMOW, ref. 52), into 1-inch round epoxy mounts. After casting, each mount was ground flat

with a rotating 9 μ m grit fixed-diamond lapping pad, then polished by a sequence of 6, 3, and 1 μ m-grit polycrystalline diamond suspensions on low-nap, rotating polishing pads. A final polish was achieved with a colloidal alumina suspension (0.05 μ m) that enhanced the quality of subsequent CLFM imaging. This second round of CLFM imaging was used to navigate and identify targets for δ_{18} O analysis by ion microprobe. Following CLFM imaging, the sample was coated with a thin layer of gold to a thickness of 60 nm in order to facilitate charge-compensation during ion microprobe analysis.

Ion microprobe analysis of speleothem calcite $\delta_{18}O$ was completed on the large-radius multi-collector CAMECA IMS 1280 secondary ion mass spectrometer in the WiscSIMS lab at University of Wisconsin-Madison. Analysis of both samples was completed over the course of five 12-hour days divided into three sessions between October 2017 and March 2018. For each session, a ~ 1.3 nA primary beam of $_{133}Cs_{+}$ ions with 20 keV impact energy was focused to a diameter of 9 μ m on the sample surface. The primary beam sputtered oval-shaped spots - 9 x 12 μ m in dimension - into the sample surface to a depth of approximately 1 μ m. Ionized components of the sputtered material ("secondary ions") were accelerated into the double-focusing mass spectrometer, which was tuned to simultaneously collect $_{16}O_{-}$, $_{18}O_{-}$, and the molecular ion species $_{16}O_{1}H_{-}$ on three Faraday cups. The resulting count rate for $_{16}O_{-}$ during calcite analyses was $\sim 2.5 \times 10^{9}$ cps.

Ion microprobe analyses are standardized using a bracketing technique whereby each group of 12-16 sample analyses is bracketed by two sets of typically 4 analyses of WiscSIMS calcite standard UWC-3. The external precision of a block of sample analyses is reported as the 2 s.d. of the (eight) bracketing standard analyses. In order to place the raw δ_{18} O values of a bracket of sample analyses onto the VSMOW scale, we use the mass bias calculated from the average raw

δ18O value of the bracketing standards. For ease of comparison, VSMOW values are converted to VPDB (53). Results of each ion microprobe analysis, including raw and standardized values, are reported in a comprehensive data table available online (SI Table S1). Post-processing and quality control of ion microprobe data are explained in detail in the SI Appendix. All speleothem data associated with the manuscript are entirely contained within the Supporting Appendix and references and will be available at the National Center for Environmental Information.

The normalized, intra-band $\delta_{18}O$ variability for each speleothem sample was plotted and binned in MATLAB (54) using the qualitative fluorescence classifications and the spot positions as measured in the open-source geographic information system, QGIS (see SI Appendix; refs 55, 56). The bootstrap randomization of the intra-band $\delta_{18}O$ data was also completed in MATLAB. For this, the $\delta_{18}O$ data for each band were randomly redistributed, then normalized and binned as done with the original data. This randomization and binning was repeated 100 times and the resulting distribution of binned averages was used to define the 95% confidence interval for randomly distributed $\delta_{18}O$ values that is illustrated in Figure S1B and S1D.

Isotope-enabled climate modeling

We performed the global rainfall isotope simulations for PH (125 ka) and PL (115 ka) with isotope-enabled isoCAM3 (57). The isotope-enabled isoCAM3 incorporates stable water isotopes into the NCAR atmospheric general circulation model CAM3 in T31 resolution with fractionation associated with surface evaporation and cloud processes (58). We ran the isotope-enabled isoCAM3 atmosphere model with boundary conditions from equilibrium coupled climate simulations from low-resolution NCAR CCSM3 (59) forced by orbital configurations and greenhouse gases at 125 ka and 115 ka, respectively. We used the same pre-industrial

surface ocean δ18O values in both PH and PL isoCAM3 simulations to isolate the fractionation associated with atmospheric processes. Figures 1-3 show precipitation and wind output from the isoCAM3 model. Ocean water δ18O in this model does not respond to runoff or meteoric water. All model output is archived on the National Center for Atmospheric Research's Campaign Storage file system and is publicly available via the NCAR Data Sharing Service (https://www2.cisl.ucar.edu/resources/storage-and-file-systems/using-the-ncar-data-sharing-service).

Acknowledgments:

The authors acknowledge B. Hess for sample preparation; J. Valley and the WiscSIMS lab; J. Fournelle, B. Schneider and the UW-Madison Wilcox SEM lab; R. Tan, L. Rodenkirch and the UW-Madison Optical Imaging Core; the University of Michigan Stable Isotope Lab. We also acknowledge high-performance computing support from Yellowstone (ark:/85065/d7wd3xhc) and Cheyenne (doi:10.5065/D6RX99HX) provided by the Computational and Information Systems Laboratory at the National Center for Atmospheric Research, sponsored by the National Science Foundation. This research used resources of the Oak Ridge Leadership Computing Facility at the Oak Ridge National Laboratory, supported by the Office of Science of the U.S. Department of Energy. Computing supported under Department of Energy Contract No. DE-AC05-00OR22725. WiscSIMS is supported by the National Science Foundation (EAR-1355590 and EAR-1658823) and UW-Madison. This research is supported by the National Science Foundation (1603065, IO+FH+GC; 1231155, IO; 1702407, IO). Sample mounts analyzed in this study are curated at the University of Wisconsin-Madison Geology Museum. The authors acknowledge with thanks the comments of anonymous reviewers that led

to substantial revision and clarification of the original manuscript.

345

346

358

359

360

361

344

References:

- 1. Stringer CB, Grün R, Schwarcz HP, Goldberg P (1989) ESR dates for the hominid burial site of Es Skhul in Israel. *Nature* 338:756–758.
- Hershkovitz I, et al. (2018) The earliest modern humans outside Africa. *Science* 359:456–459.
- 35. Roberts N (2014) *The Holocene: An Environmental History* (John Wiley & Sons, Incorporated).
- 4. Kennett DJ, Kennett JP (2006) Early state formation in southern mesopotamia: Sea levels, shorelines, and climate change. *J Isl Coast Archaeol* 1(1):67–99.
- 5. Bar-Matthews M, Ayalon A, Kaufman A (2000) Timing and hydrological conditions of Sapropel events in the Eastern Mediterranean, as evident from speleothems, Soreq cave, Israel. *Chem Geol* 169(1–2):145–156.
 - 6. Bar-Matthews M, Ayalon A, Gilmour M, Matthews A, Hawkesworth CJ (2003) Sea land oxygen isotopic relationships from planktonic foraminifera and speleothems in the Eastern Mediterranean region and their implication for paleorainfall during interglacial intervals. *Geochim Cosmochim Acta* 67(17):3181–3199.
- Bar-Matthews M, Keinan J, Ayalon A (2019) Hydro-climate research of the late
 Quaternary of the Eastern Mediterranean-Levant region based on speleothems research –
 A review. *Quat Sci Rev* 221(105872). doi:10.1016/j.quascirev.2019.105872.
- 365 8. Grant KM, et al. (2012) Rapid coupling between ice volume and polar temperature over 366 the past 150,000 years. *Nature* 491(7426):744–7.

- 9. Rossignol-Strick M, Nesteroff W, Olive P, Vergnaud-Grazzini C (1982) After the deluge:
 Mediterranean stagnation and sapropel formation. *Nature* 295:105–110.
- Rohling EJ, Marino G, Grant KM (2015) Mediterranean climate and oceanography, and the periodic development of anoxic events (sapropels). *Earth-Science Rev* 143:62–97.
- 11. Rossignol-Strick M, Paterne M (1999) A synthetic pollen record of the eastern

 Mediterranean sapropels of the last 1 Ma: Implications for the time-scale and formation of

 sapropels. *Mar Geol* 153(1–4):221–237.
- 374 12. Grant KM, et al. (2016) The timing of Mediterranean sapropel deposition relative to 375 insolation, sea-level and African monsoon changes. *Quat Sci Rev* 140:125–141.
- 13. Enzel Y, et al. (2008) The climatic and physiographic controls of the eastern

 Mediterranean over the late Pleistocene climates in the southern Levant and its

 neighboring deserts. *Glob Planet Change* 60:165–192.
- Dansgaard W (1964) Stable isotopes in precipitation. *Tellus* 16(4):436–468.
- 15. Kutzbach JE (1981) Monsoon climate of the Early Holocene: Climate experiment with the Earth's orbital parameters for 9000 years ago. *Science* 214:59–61.
- Wang YJ, et al. (2001) A high-resolution absolute-dated late Pleistocene Monsoon record from Hulu Cave, China. *Science* 294(5550):2345–2348.
- 17. Cheng H, Sinha A, Wang X, Cruz FW, Edwards RL (2012) The Global Paleomonsoon as seen through speleothem records from Asia and the Americas. *Clim Dyn* 39(5):1045–1062.
- 18. Cheng H, et al. (2012) The climatic cyclicity in semiarid-arid central Asia over the past 500,000 years. *Geophys Res Lett* 39(1):L01705.
- Fleitmann D, et al. (2011) Holocene and Pleistocene pluvial periods in Yemen , southern

- 390 Arabia. *Quat Sci Rev* 30(7–8):783–787.
- 391 20. Fleitmann D, Burns SJ, Neff U, Mangini A (2003) Changing moisture sources over the
 last 330,000 years in Northern Oman from fluid-inclusion evidence in speleothems. *Quat*393 *Res* 60:223–232.
- Waldmann N, Torfstein A, Stein M (2010) Northward intrusions of low- and mid-latitude storms across the Saharo-Arabian belt during past interglacials. *Geology* 38(6):567–570.
- Torfstein A, et al. (2015) Dead Sea drawdown and monsoonal impacts in the Levant during the last interglacial. *Earth Planet Sci Lett* 412:235–244.
- Kutzbach JE, Chen G, Cheng H, Edwards RL, Liu Z (2014) Potential role of winter
 rainfall in explaining increased moisture in the Mediterranean and Middle East during
 periods of maximum orbitally-forced insolation seasonality. *Clim Dyn* 42(3–4):1079–
 1095.
- McGarry S, et al. (2004) Constraints on hydrological and paleotemperature variations in
 the Eastern Mediterranean region in the last 140ka given by the δD values of speleothem
 fluid inclusions. *Quat Sci Rev* 23(7–8):919–934.
- Vaks A, Bar-Matthews M, Matthews A, Ayalon A, Frumkin A (2010) Middle-Late
 Quaternary paleoclimate of northern margins of the Saharan-Arabian Desert:
 Reconstruction from speleothems of Negev Desert, Israel. *Quat Sci Rev* 29(19–20):2647–2662.
- Orland IJ, et al. (2009) Climate deterioration in the Eastern Mediterranean as revealed by
 ion microprobe analysis of a speleothem that grew from 2.2 to 0.9 ka in Soreq Cave,
 Israel. Quat Res 71(1):27–35.
- Orland IJ, et al. (2012) Seasonal resolution of Eastern Mediterranean climate change since

- 34ka from a Soreq Cave speleothem. *Geochim Cosmochim Acta* 89:240–255.
- 414 28. Ayalon A, Bar-Matthews M, Sass E (1998) Rainfall-recharge relationships within a
- karstic terrain in the Eastern Mediterranean semi-arid region, Israel: δ18O and δD
- characteristics. *J Hydrol* 207:18–31.
- 29. Orland IJ, et al. (2014) Seasonal climate signals (1990–2008) in a modern Soreq Cave
- stalagmite as revealed by high-resolution geochemical analysis. *Chem Geol* 363:322–333.
- 30. Kaufman A, Bar-Matthews M, Ayalon A, Carmi I (2003) The vadose flow above Soreq
- Cave, Israel: a tritium study of the cave waters. *J Hydrol* 273(1–4):155–163.
- 31. Tyrlis E, Lelieveld J, Steil B (2013) The summer circulation over the eastern
- Mediterranean and the Middle East: Influence of the South Asian monsoon. *Clim Dyn*
- 423 40(5–6):1103–1123.
- 424 32. Mohtadi M, Prange M, Steinke S (2016) Palaeoclimatic insights into forcing and response
- of monsoon rainfall. *Nature* 533(7602):191–199.
- 33. Battisti DS, Ding Q, Roe GH (2014) Coherent pan-Asian climatic and isotopic response to
- orbital forcing of tropical insolation. *J Geophys Res* 119(21):11,997-12,020.
- 428 34. Bosmans JHC, et al. (2015) Precession and obliquity forcing of the freshwater budget over
- the Mediterranean. *Quat Sci Rev* 123:16–30.
- 35. Tzedakis PC (2007) Seven ambiguities in the Mediterranean palaeoenvironmental
- 431 narrative. *Quat Sci Rev* 26(17–18):2042–2066.
- 432 36. Arz HW, Lamy F, Pätzold J, Müller PJ, Prins M (2003) Mediterranean Moisture Source
- for an Early-Holocene Humid Period in the Northern Red Sea. *Science* 300:118–121.
- 434 37. Langgut D, Almogi-Labin a., Bar-Matthews M, Weinstein-Evron M (2011) Vegetation
- and climate changes in the South Eastern Mediterranean during the Last Glacial-

- Interglacial cycle (86 ka): new marine pollen record. *Quat Sci Rev* 30(27–28):3960–3972.
- 38. Cheddadi R, Rossignol-Strick M (1995) Eastern Mediterranean Quaternary paleoclimates
- from pollen and isotope records of marine cores in the Nile Cone Area. *Paleoceanography*
- 439 10(2):291–300.
- 39. Develle A, et al. (2011) A 250 ka sedimentary record from a small karstic lake in the
- Northern Levant Paleoclimatic implications. *Palaeogeogr Palaeoclimatol Palaeoecol*
- 442 305(1-4):10-27.
- 40. Mehterian S, et al. (2017) Speleothem records of glacial/interglacial climate from Iran
- forewarn of future Water Availability in the interior of the Middle East. *Quat Sci Rev*
- 445 164:187–198.
- 41. Rosenberg TM, et al. (2011) Humid periods in southern Arabia: Windows of opportunity
- for modern human dispersal. *Geology* 39(12):1115–1118.
- 448 42. Tierney JE, deMenocal PB, Zander PD (2017) A climatic context for the out-of-Africa
- migration. Geology 45(11):1023–1026.
- 43. Prell WL, Kutzbach JE (1987) Monsoon variability over the past 150,000 years. J
- 451 *Geophys Res* 92(D7):8411.
- 452 44. de Noblet N, Braconnot P, Joussaume S, Masson V (1996) Sensitivity of simulated Asian
- and African summer monsoons to orbitally induced variations in insolation 126, 115 and 6
- 454 kBP. Clim Dyn 12:589–603.
- 45. Herold M, Lohmann G (2009) Eemian tropical and subtropical African moisture transport:
- an isotope modelling study. *Clim Dyn* 33:1075–1088.
- 457 46. Frumkin A, Bar-Yosef O, Schwarcz HP (2011) Possible paleohydrologic and
- 458 paleoclimatic effects on hominin migration and occupation of the Levantine Middle

- 459 Paleolithic. *J Hum Evol* 60(4):437–451.
- 460 47. Vaks A, et al. (2007) Desert speleothems reveal climatic window for African exodus of early modern humans. *Geology* 35:831–834.
- 48. Boivin N, Fuller DQ, Dennell R, Allaby R, Petraglia MD (2013) Human dispersal across diverse environments of Asia during the Upper Pleistocene. *Quat Int* 300:32–47.
- 49. Drake NA, Blench RM, Armitage SJ, Bristow CS, White KH (2010) Ancient watercourses and biogeography of the Sahara explain the peopling of the desert. *Proc Natl Acad Sci* 108(2):458–462.
- 50. Kutzbach JE, Liu X, Liu Z, Chen G (2008) Simulation of the evolutionary response of global summer monsoons to orbital forcing over the past 280,000 years. *Clim Dyn*30(6):567–579.
- 51. Orland IJ, et al. (2015) Direct measurements of deglacial monsoon strength in a Chinese stalagmite. *Geology* 43(6):555–558.
- 52. Kozdon R, Ushikubo T, Kita NT, Spicuzza M, Valley JW (2009) Intratest oxygen isotope variability in the planktonic foraminifer N. pachyderma: Real vs. apparent vital effects by ion microprobe. *Chem Geol* 258(3–4):327–337.
- 53. Coplen TB, Kendall C, Hopple J (1983) Comparison of stable isotope reference samples.

 Nature 302:236–238.
- 477 54. MATLAB (2018).
- 478 55. QGIS Development Team (2018) QGIS Geographic Information System.
- Linzmeier B, Kitajima K, Denny A, Cammack J (2018) Making Maps on a Micrometer
 Scale. *Eos (Washington DC)* 99:24–28.
- Liu Z, et al. (2014) Chinese cave records and the East Asia Summer Monsoon. *Quat Sci*

482	Rev	83:115-128.

489

- 58. Noone D, Sturm C (2010) Comprehensive dynamical models of global and regional water isotope distributions. *Isoscapes: Understanding Movement, Pattern, and Process on Earth Through Isotope Mapping*, eds West JB, Bowen GJ, Dawson TE, Tu KP (Springer Netherlands, Dordrecht), pp 195–219.
- 487 Yeager SG, Shields CA, Large WG, Hack JJ (2006) The low-resolution CCSM3. *J Clim*488 19:2545–2566.

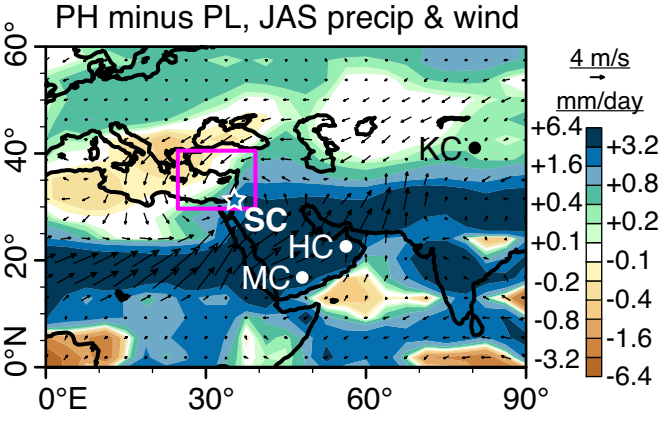
Figure Legends:

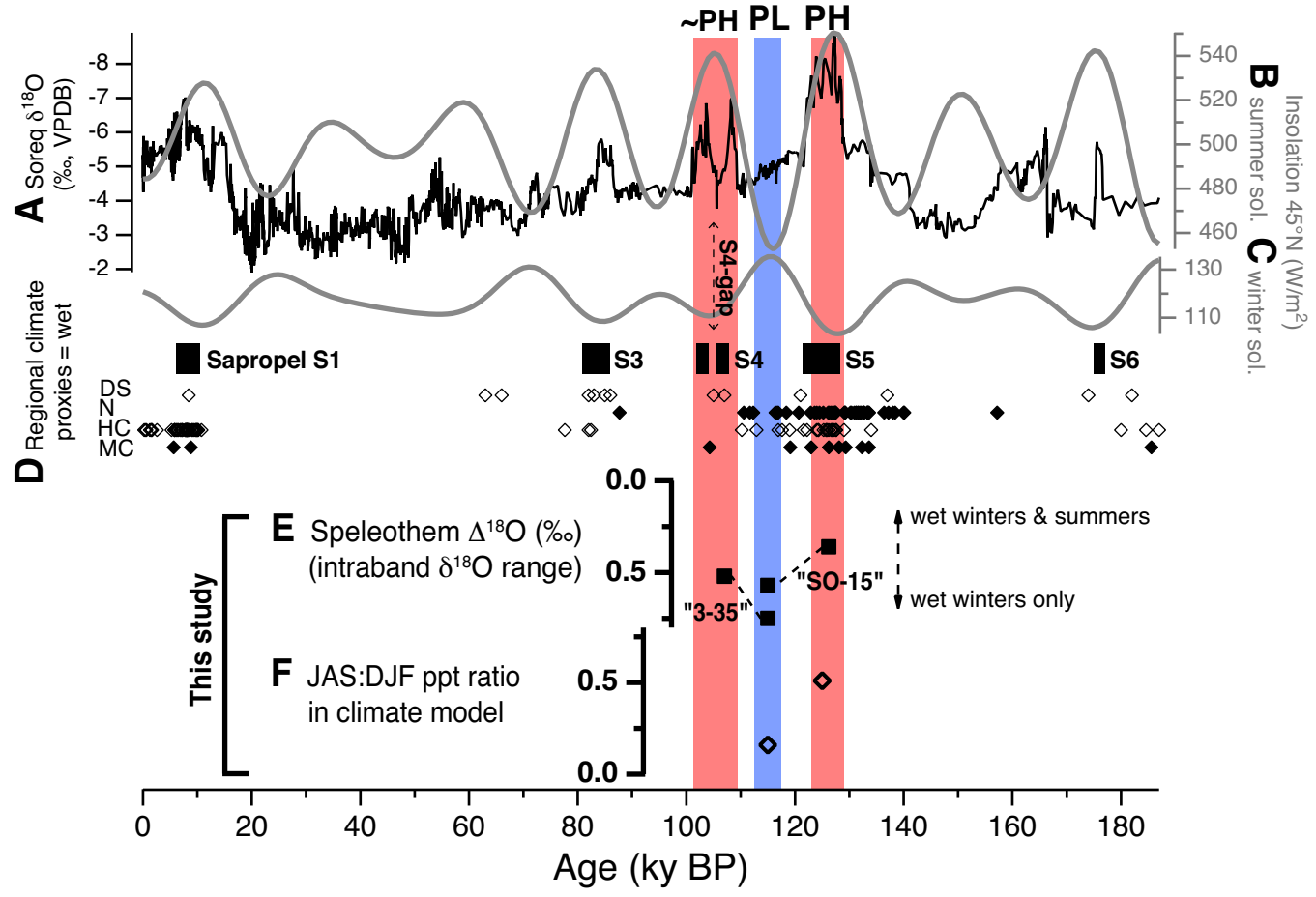
Figure 1: Model results showing changes in summer (JAS) precipitation amount (mm/day; note the logarithmic color scale) at 125 ka (PH, maximum summer insolation) relative to 115 ka (PL, minimum summer insolation) and associated changes in the speed (m/s) and direction of surface winds. Superimposed are the locations of Soreq Cave in Israel (SC, star), the geographic region examined in this and earlier global climate simulations (23) (pink rectangle), and the locations of paleoclimate records referenced in the text (Kesang Cave, KC; Hoti Cave, HC; Mukalla Cave, MC). The locations of paleoclimate records from the Dead Sea and the Negev Desert overlap with the star symbol.

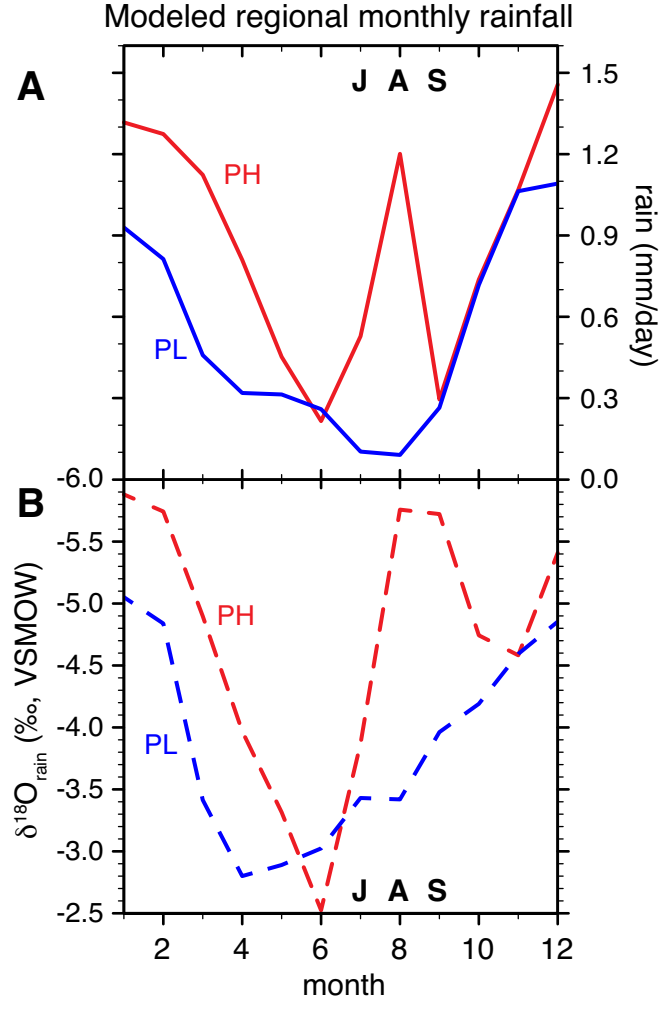
Figure 2: Multi-plot of (A) the composite Soreq Cave δ18O record since 185 ka (7, 8) (note the inverted axis), (B) 45°N summer solstice and (C) winter solstice insolation, with bars highlighting PH, PL and the PH analog, ~PH. The timing of EM sapropel formation (D) in response to increased African monsoon rainfall (11, 12) is shown along with a prominent interruption of sapropel event 4 (S4-gap). Also presented are regional hydroclimate proxy indications of increased moisture near the Dead Sea (DS) (21), Negev Desert (N) (25), and at two caves on the Arabian Peninsula (HC & MC after Figure 1) (19, 20). From this study (E), the mean seasonal δ18O range (Δ18O; inverted axis) measured in two Soreq speleothems ("SO-15" and "3-35") is plotted for PH, PL, and ~PH time periods. The modeled ratio of summer (JAS) to winter (DJF) precipitation amount is illustrated (F) for the EM study region outlined in Figure 1.

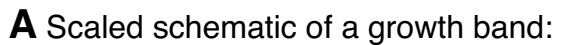
Figure 3: Modeled monthly rainfall totals (A) and δ_{18} O of rainfall (B) in PH (red) vs. PL (blue) simulations. Summer months are labeled JAS. Note inverted δ_{18} O axis.

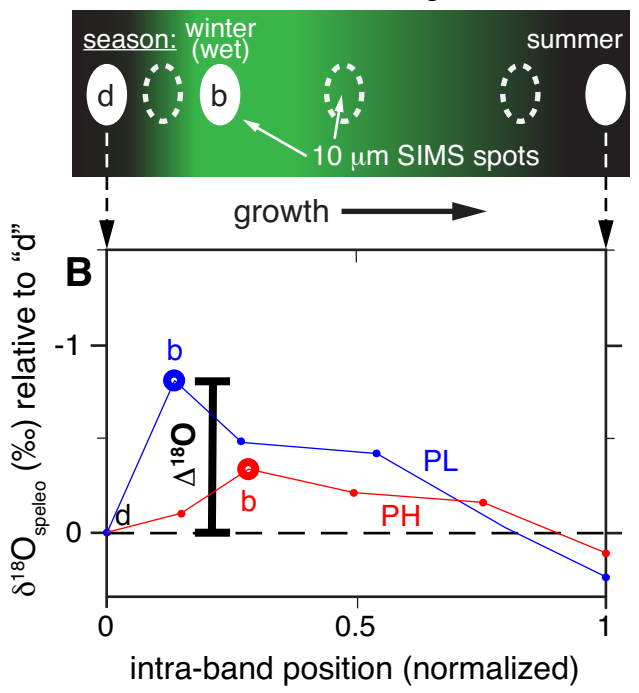
Figure 4: Summary of intra-band speleothem δ_{18} O variability. (A) Scaled schematic of SIMS spots in dark ("d"; summer "baseline" dripwater) and bright ("b"; winter wet season dripwater) fluorescent portions of a speleothem growth band, with 3-10 spots in each band (including the dark spot "d" at the end of the preceding band). (B) Intra-band δ_{18} O variability relative to "d" in two representative growth bands from Soreq speleothem "SO-15". The horizontal axis is scaled from the end of the preceding band (=0) to the end of the current band (=1). Values of δ_{18} O measured in each band (small circles) are connected by red (PH) or blue (PL) lines. Large circles mark the SIMS spot "b" in the bright fluorescent portion of each band and are the lowest δ_{18} O value measured in each band (note the inverted vertical axis). Calculation of Δ_{18} O is illustrated for a single band and is the difference in the δ_{18} O of the "b" and "d" spots. (C) For both Soreq speleothems analyzed in this study, measured Δ_{18} O values are plotted for both PL (blue circles) and PH (red) periods. To help visualize differences between Δ_{18} O in each insolation scenario, mean values are marked with a horizontal line and the probability density (with gaussian kernel) is illustrated with a gray envelope.



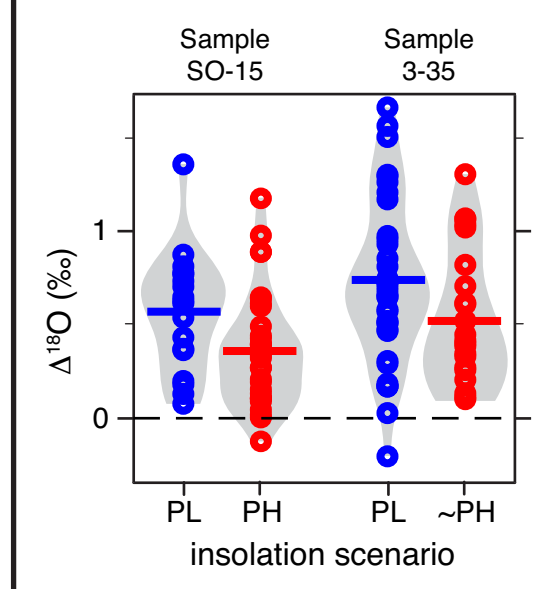








C Lower Δ^{18} O measured at PH $[\Delta^{18} \mathbf{O} = \delta^{18} \mathbf{O}_{\mathrm{speleo,d}} - \delta^{18} \mathbf{O}_{\mathrm{speleo,b}}]$





Supplementary Information for

Resolving seasonal rainfall changes in the Middle East during the last interglacial period

Ian J. Orland, Feng He, Miryam Bar-Matthews, Guangshan Chen, Avner Ayalon, John E. Kutzbach

Corresponding author: Ian J. Orland

Email: orland@wisc.edu

This PDF file includes:

Supplementary text Figs. S1 to S8 Caption for dataset Table S1 References for SI reference citations

Other supplementary materials for this manuscript include the following:

Dataset Table S1

Supplementary Information Text

Extended Materials and Methods

Post-processing of ion microprobe analyses. Following ion microprobe analysis, an additional thin (~10 nm) gold coat was applied to each sample mount so that the pit-bottoms could be imaged by scanning electron microscope (SEM). Using the approach detailed in another study (1), each pit was examined and classified – independently of ion microprobe results – as either "regular" (n=602), "intermediate" (n=9), or "irregular" (n=0). These classifications are listed for each spot in Table S1. Intermediate and irregular pits contain scratches and/or void spaces that could compromise the sputtering process and bias the isotopic measurement. No irregular pits were observed. Additional quality control metrics, outlined below, were used to evaluate the data from regular and intermediate pits.

For each ion microprobe analysis, two metrics were monitored as quality controls. The first is "relative yield", where the yield (secondary ¹⁶O cps/primary beam intensity) of each sample analysis is divided by the average yield of the bracketing standards (% units). The second metric is the background-corrected OH/O ratio, which is interpreted as an empirical indicator of water and/or organic content in low-temperature carbonates measured by ion microprobe (2, 3). For each metric, statistical outliers were identified using the Tukey outlier definition (4) and those spots were removed from further consideration in the manuscript (n=10).

Following the quality control assessments, the gold coating was removed from each sample mount with 0.25 μ m polycrystalline diamond suspension so that the analysis transects could be re-imaged by confocal laser fluorescent microscopy (CLFM). We note, however, that the ~1 μ m depth of ion microprobe pits means that the gold coating in the bottom of the pits is not removed by the diamond suspension. Conveniently, the remnant gold reflects the excitation laser during CLFM imaging so that the location of each ion microprobe analysis is clearly evident as a black spot in the fluorescent image. In this manner, each spot could be qualitatively classified for its position in the fluorescent banding: "bright" spots in the brightest fluorescent portion of a band, "dark" spots in the darkest portion of a band, and all other spots unclassified. The fluorescent images and spot classifications were then combined with ion microprobe results into a microspatial database to facilitate data visualization and accurate age model construction.

Following guidelines established at the WiscSIMS lab, the open-source geographic information system software QGIS was used to generate a microspatial database that integrated imaging, ion microprobe, quality control, and qualitative classification data layers (5, 6). Scanned images of the flattened, but uncut, samples alongside a ruler were used as the spatial reference frame and scaled so that the nominal unit of distance is 1 μ m (vs. 1m in typical GIS applications). Higher magnification images with smaller fields of view (e.g. CLFM images) were then oriented onto the reference image, followed by the ion microprobe spot data. One of the advantages of this approach is that it greatly improves the process for developing an age model for microanalytical data. Within the spatial database, a reference line was drawn over the sample images following the analytical traverse along a calcite growth axis. A large, static image of the spatial database for each sample – including fluorescent imaging, labeled ion microprobe spot positions and δ^{18} O values, and reference line – is available as Figures S3 and S4. For each ion microprobe spot, the distance along the line (i.e. growth axis) is reported as the point of closest-location (6) and

recorded in Table S1. These distance values are used to calculate the relative position of each spot both within the sample and within its fluorescent growth band.

Age model. The location of U-Th ages from these samples (7–9) are also mapped onto the spatial database. The positions of each age along the same reference line described above are used to construct an age model for the ion microprobe analyses in sample 3-35 (SI Table S1) based on a Bayesian model for deposition (OxCal(ref. 10) version 4.3). For sample SO-15, the portion analyzed in this study is a subsample from between (but not including) two U-Th ages. Given the purpose of this study and the distinct pattern of high-amplitude, low-frequency δ^{18} O variability within both samples, ion microprobe analyses were then binned into either PH, PL, ~PH, or S4-gap periods based on both age and band-average δ^{18} O values. A δ^{18} O difference of >2% clearly separates the binned analyses from both samples (lower δ^{18} O = PH); unbinned bands have intermediate ages and δ^{18} O values.

Statistical analysis. The two-sample Kalmogorov-Smirnov (K-S) test evaluates the null hypothesis that two samples are drawn from the same distribution. The K-S statistic, D, describes the difference between the one-dimensional empirical distribution function of each sample. The null hypothesis is rejected when D is larger than a reference value that scales with the significance level (p-value). For speleothem SO-15, D = 0.4316 for the PH (n=30) and PL (n=19) Δ^{18} O values and rejects the null-hypothesis at p = 0.018. For speleothem 3-35, D = 0.4119 for the ~PH (n=24) and PL (n=35) Δ^{18} O values and rejects the null-hypothesis at p = 0.011.

The standard two-sample t-test evaluates the null hypothesis that two samples with assumed equal variance have the same mean. Here, given the result of the preceding K-S tests that suggest the Δ^{18} O values from PH and PL are not from the same distribution, a variation of the two-tailed t-test (sometimes called Welch's t-test) is used where it is assumed that the sample distributions have unknown and unequal variances. For this test, effective degrees of freedom are calculated using Satterthwaite's approximation. For speleothem SO-15, the null hypothesis is rejected for PH (n=30) and PL (n=19) Δ^{18} O values at p = 0.026, t-value = 2.312, degrees of freedom = 37.26. For speleothem 3-35, the null hypothesis is rejected for ~PH (n=24) and PL (n=35) Δ^{18} O values at p = 0.029, t-value = 2.242, degrees of freedom = 55.10.

Extended Model Results

Alternative geographic boundaries. The rainfall-isotope model results reported in Figs. 2 and 3 are integrated – by design – from the same region investigated by Kutzbach et al. (2014; ref. 11). Here, we demonstrate that the seasonal rainfall response presented in the manuscript is regionally robust by examining results from an overlapping, land-dominated area of the Middle East (Fig. S5). The modeled rainfall from this region (Fig. S6) follows the same patterns of seasonal change as shown in Fig. 3. This reinforces the three main seasonal responses observed in the original study area: 1) rainfall amount during PH is greater than PL during both winter and summer months, 2) the largest increase in rainfall occurs in summer months that are dry during PL, and 3) the summer monsoon rainfall added during PH has similar low- δ^{18} O values to winter rainfall.

The differences in the relative seasonal changes between the two regions are a logical outcome. Westerly-driven winter moisture is less pronounced in the eastern test region, and this region also captures the geographic corridor of greatest northward summer monsoon expansion (Fig. S5). In both regions, however, the amount-weighted decrease of δ^{18} O in PH versus PL is larger in summer than in winter. The model result from each area points to the regional tendency at PH for additional low- δ^{18} O summer monsoon rains to decrease the seasonal δ^{18} O gradient recorded in Soreq Cave speleothems, even if winter rainfall also increased.

Evaporation. Evaporation of surface and/or groundwater could theoretically alter the amount of infiltration and/or the $\delta^{18}O$ of dripwater in Soreq Cave. Here we provide an overview of evidence from the climate model used in this study and dripwater observations in the modern cave that argue against evaporation as the cause for the observed difference in $\Delta^{18}O$ between PH and PL. First, the modeled balance of evaporation and precipitation changes very little between PH and PL. Figure S7 illustrates this balance as E-ppt (dashed lines, mm/day) in a plot of the monthly modeled hydrograph for the land-dominated region that includes the Levant shown in Fig. S5. We note that while the representation of evaporation in the climate model is necessarily simplified and cannot account for e.g. the efficiency of groundwater infiltration in fractured bedrock, that nevertheless the regional and seasonal similarity of E-ppt in PH and PL simulations is instructive. E-ppt during summer and winter wet seasons in PH is similar to that in the winter wet season of PL (a modern analog). A similar comparison for the study region in Fig. 1 is not useful for our purposes because evaporation from water-dominated EM grid cells dominates the surface water flux.

In the cave, modern observations of year-round dripwater in Soreq Cave do not show isotopic evidence of evaporation (i.e. enrichment of the heavier 2H and ^{18}O isotopes), which would move dripwater off of the local Mediterranean Meteoric Water Line (12). Dripwaters are interpreted as being sourced from efficient infiltration of groundwater that avoids substantial evaporation either at the surface or in the subsurface. Together with the E-ppt output from the model, these observations suggest that dripwater at PH would infiltrate as in the modern cave and not have an isotopic signature of evaporation. Moreover, if there were no summer monsoon rainfall at PH but elevated summertime evaporation did induce ^{18}O -enrichment of groundwater above Soreq Cave, the effect would be to increase the $\delta^{18}O$ of non-winter "slow drip" or "baseline" dripwater (12, 13) and thus increase $\Delta^{18}O$. Therefore, given modern observations at the cave and the model output of a similar evaporation-precipitation balance at PH and PL, the available evidence does not indicate that evaporation could cause $\Delta^{18}O$ to be smaller at PH than PL.

Extended Discussion

Seasonal variability of δ^{18} O in and above Soreg Cave. Prior monitoring of rainwater and dripwater at Soreq Cave are the foundation for our interpretation of the hydrological system that supplies dripwater to the cave. Parallel collection of rainwater and dripwater at Soreq over sequential years identified that average monthly rainfall δ^{18} O values are inversely correlated so that, generally, during the wettest months (winter) the average δ^{18} O of monthly precipitation is lowest (12, 14). Notably, in the modern climate while there is little rain during summer months above the cave, dripping continues in the cave. Dripwater δ^{18} O in the cave follows a similar pattern of seasonal variability to rainfall δ^{18} O, but with a smaller range of δ^{18} O values. Lowest dripwater δ^{18} O occurs when driprates are highest in the wet winter months ("fast dripwaters") and empirically track the annually averaged δ^{18} O of rainfall above the cave (12, 13). As introduced in the last section, during non-winter months when driprates are slower the dripwater δ^{18} O is consistently higher. Prior studies suggest that some vadose zone groundwater has a residence time of 2-3 decades (15) and that this mixed source of "baseline" dripwater is derived from rainfall events of intermediate amount (10-20 mm) with relatively high δ^{18} O values in the shoulder seasons before and after the winter wet season (12). Together, these Soreq Cave dripwater observations are interpreted to reflect a two-reservoir mixing model where a "baseline" dripwater reservoir is overprinted seasonally by lower- δ^{18} O "fast dripwaters" that are delivered along more direct conduits during the winter wet season (12–14).

Micro-analysis of Soreq Cave speleothems indicates that seasonal $\delta^{18}O$ variability of dripwater is recorded within annual growth bands that are delineated by fluorescent banding. A regular pattern of $\delta^{18}O$ variability was first observed in a Soreq speleothem across the fluorescent banding of a Late Holocene stalagmite (13), and again in a stalagmite that grew during the last deglaciation (16). These studies interpreted the bright- and dark-fluorescent couplets that form each growth band to reflect the "fast" and "baseline" dripwater reservoirs, respectively; the fluorescence is caused by organic material that was inferred to be transported from overlying soils along more direct conduits with elevated groudwater flux. The fluorescent portion of each band in Holocene growth consistently had the lowest $\delta^{18}O$ value indicating that it represented calcite growth from the winter wet season (13, 16). Multi-proxy micro-analysis of a modern stalagmite corroborated this interpretation and showed that, indeed, seasonal geochemical variability in a Soreq speleothem reflected observed changes in rainfall amount measured at the surface (1).

For the samples measured in the present study, we assume the same empirical groundwater mixing model as above. Figure S8 shows non-normalized intra-band δ^{18} O variability (on the VPDB scale) for each band measured in both samples. The dark-fluorescent calcite and associated δ^{18} O measurements (at normalized positions 0 and 1 in Figure S8) are inferred to reflect the "baseline" dripwater reservoir, while the δ^{18} O measured in the bright-fluorescent portion of bands (large circles in Figure S8) reflects winter wet season dripwater. Figures S1 and 4B normalize intra-band δ^{18} O variability relative to "baseline" to better illustrate and compare the magnitude of seasonal changes. We hypothesize that summer monsoon rainfall at PH would be incorporated into "baseline" dripwater in a manner akin to the modern shoulder-season rains. Adding the low- δ^{18} O summer monsoon rain to the "baseline" would lower its relative δ^{18} O value and thus decrease Δ^{18} O. As detailed in the prior study of a modern Soreg speleothem (1) and supported by other targeted studies in the cave (17, 18), an important assumption is that speleothem δ^{18} O reflects near-equilibrium of calcite and dripwater isotopic compositions. Prior work also found that seasonal variation of drip-rates and/or growth-rates could not impart the seasonal range of δ^{18} O measured in Soreg speleothems (1). It is plausible, however, that lower average Δ^{18} O at PH could indicate faster growth (which lowers δ^{18} O) of non-winter calcite but we do not see evidence for this change in the banding (Figures S3, S4).

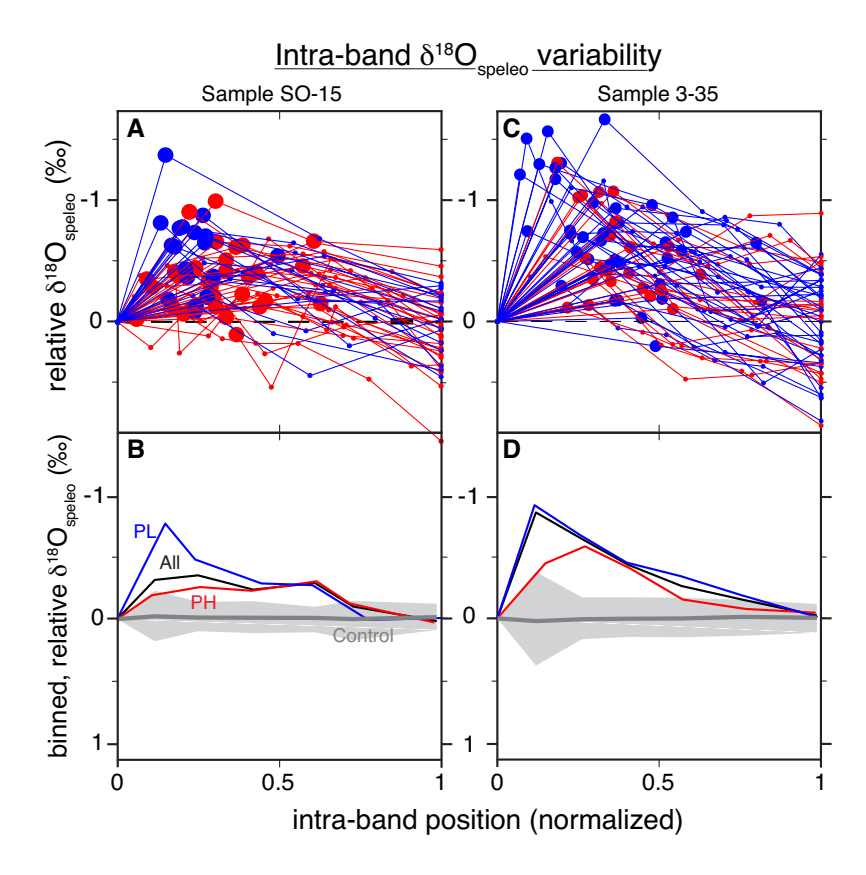


Fig. S1. Intra-band $\delta^{18}O$ data on a normalized position scale from samples SO-15 and 3-35. Axes as in Figure 4B. In panels A and C, relative $\delta^{18}O$ values (circles) from the same band are connected by a colored line (PH = red, PL = blue) with the spots placed in bright fluorescent domains plotted as large circles as in Figure 4B. In panels B and D, the positional and $\delta^{18}O$ data from panels A and C are averaged in 6 equal-width bins for PH (red line), PL (blue), and all bands (black) for the sole purpose of testing the null hypothesis that intra-band $\delta^{18}O$ variability is random. The gray line ("control") delineates the binned pattern (with a 95% confidence envelope) of data generated by a bootstrapped randomization. Because the binned patterns of PH and PL lie outside the randomization envelope, the null hypothesis that intra-band $\delta^{18}O$ variability is random is rejected.



Fig. S2. Scanned image of samples SO-15 (vertical cross-section) and 3-35 (horizontal cross-section) analyzed in this study. The samples have been cut into 1.5 cm-long blocks along the analytical traverse to be prepared for ion microprobe analysis. Growth direction of each sample is indicated. Red boxes outline the areas analyzed in this study and indicate the approximate field of view of the QGIS spatial database shown in SI Figures S3 and S4. Note ruler for scale.



Fig. S3 (above). Screengrab images of the QGIS database for sample SO-15 that include CLFM images, ion microprobe spot locations (sized $8x11\mu m$) with labels that reference the analysis number in Table S1, ion microprobe $\delta^{18}O$ values (spot color: red = low $\delta^{18}O$, blue = high $\delta^{18}O$), and reference transect (yellow).

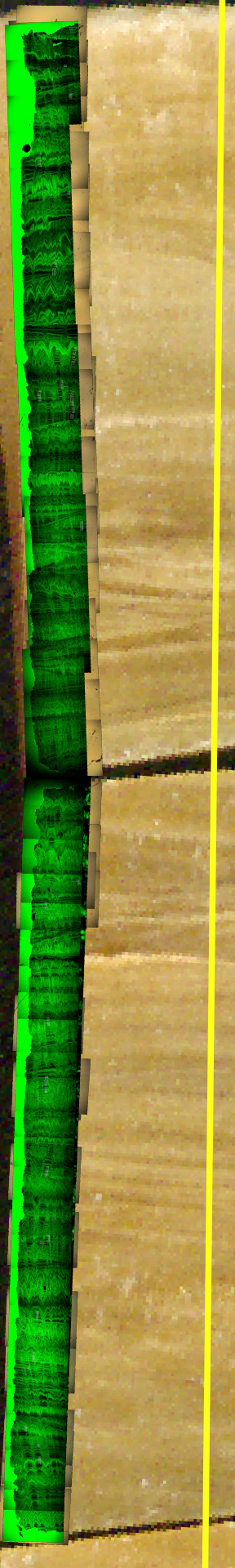


Fig. S4 (above). Screengrab images of the QGIS database for sample 3-35 that include CLFM images, ion microprobe spot locations (sized $8x11\mu m$) with labels that reference the analysis number in Table S1, ion microprobe $\delta^{18}O$ values (spot color: red = low $\delta^{18}O$, blue = high $\delta^{18}O$), and reference transect (yellow).

PH minus PL, JAS precip & wind 60°N mm/day +6.4 40° +1.6 +0.8 +0.4 +0.2 +0.1 20° -0.1 MC• -0.2 -0.4 -0.8 -1.6 30° 60° 90°E 0°

Fig. S5. Copy of Fig. 1 that shows the geographic region of isoCAM3 model output examined in the manuscript (pink box) and the region discussed in the SI Appendix and illustrated in Fig. S6 (yellow box).

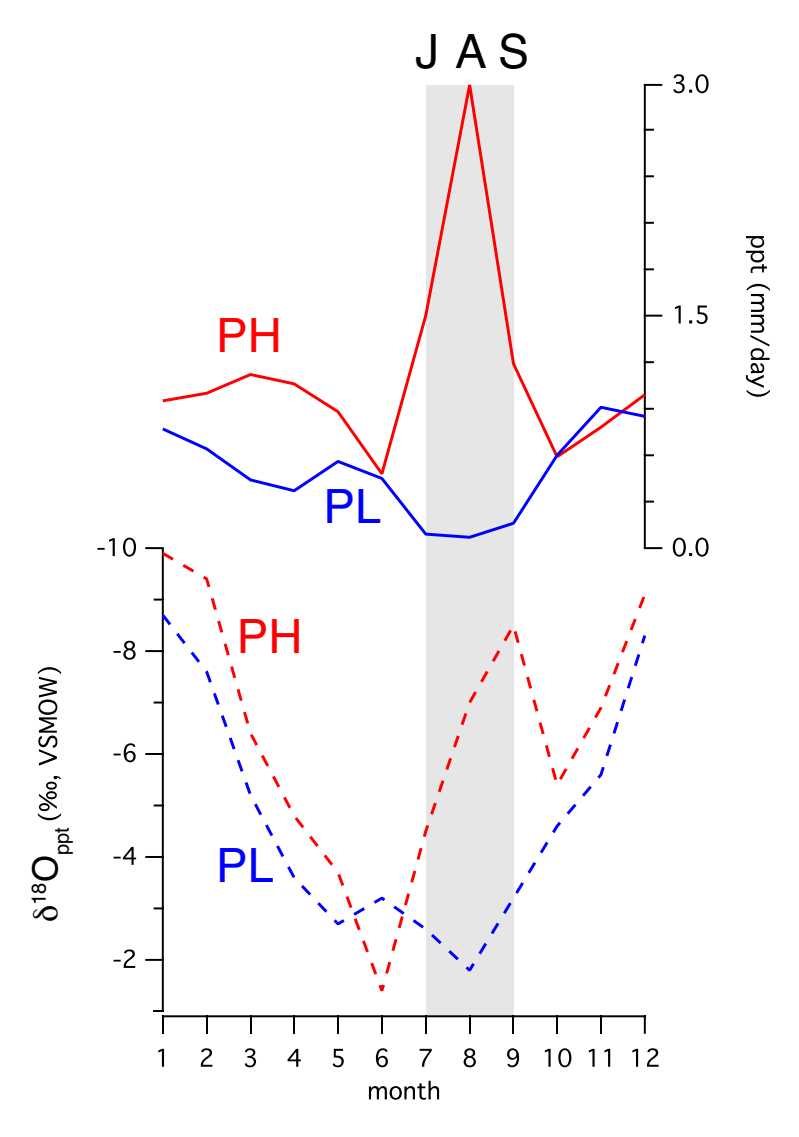


Fig. S6. Modeled monthly rainfall totals (top) and $\delta^{18}O$ of rainfall (bottom) in PH (red) vs. PL (blue) simulations for the land-dominated region outlined in yellow in Figs. S5. Summer months are labeled JAS. Note inverted $\delta^{18}O$ axis.

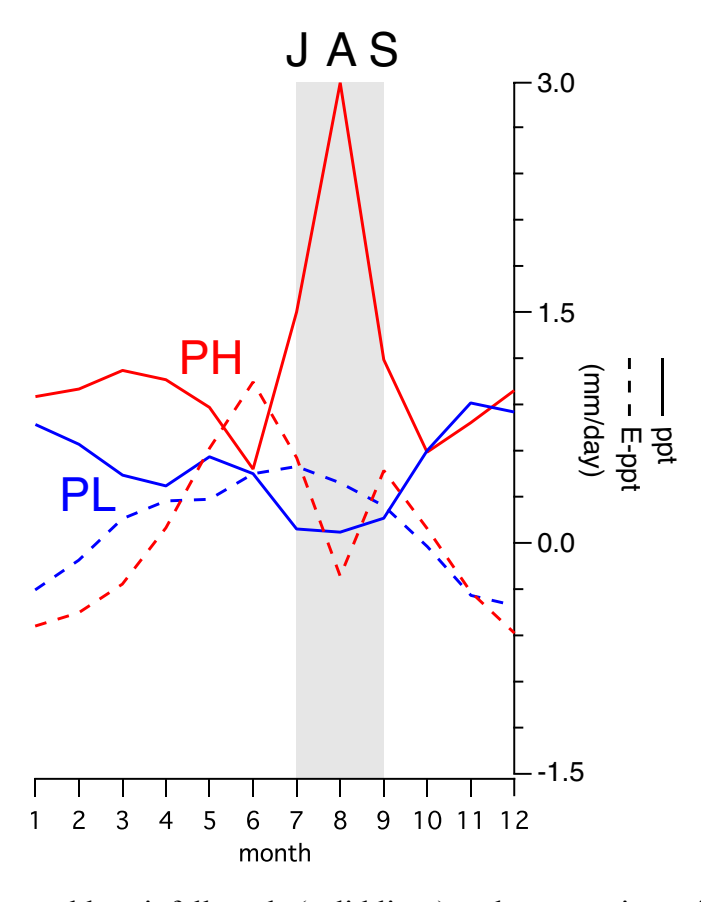


Fig. S7. Modeled monthly rainfall totals (solid lines) and evaporation-minus-precipitation (dashed lines, E-ppt) in PH (red) vs. PL (blue) simulations for the land-dominated region outlined in yellow in Fig. S5. Summer months are labeled JAS.

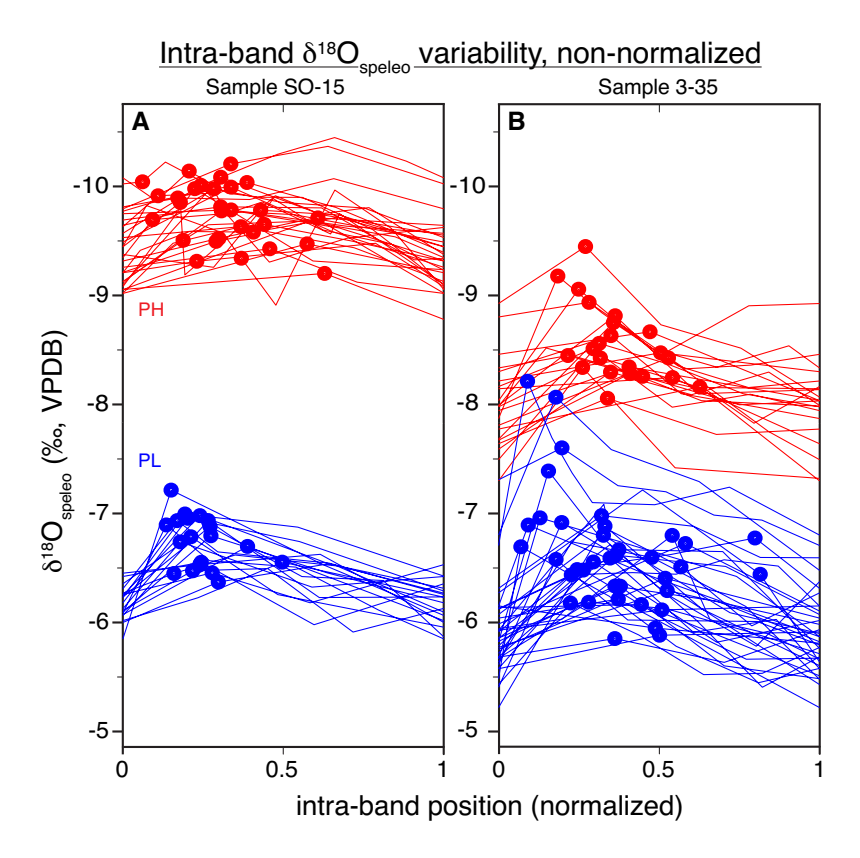


Fig. S8. Intra-band $\delta^{18}O$ data on a normalized position scale from samples SO-15 (panel A) and 3-35 (panel B), but a non-normalized vertical axis ($\delta^{18}O$; ‰, VPDB). Symbols as in Figs. 4B & S1; large circles delineate analyses in the bright fluorescent domain of each band.

Additional data Table S1 (separate file)

Raw and corrected ion microprobe $\delta^{18}O$ data and quality control metrics, profile distances generated in QGIS, age assignments, $\Delta^{18}O$ values, and plotting references.

References

- 1. Orland IJ, et al. (2014) Seasonal climate signals (1990–2008) in a modern Soreq Cave stalagmite as revealed by high-resolution geochemical analysis. *Chem Geol* 363:322–333.
- Orland IJ, et al. (2015) Enhancing the accuracy of carbonate δ^{18} O and δ^{13} C measurements by SIMS. *American Geophysical Union Fall Meeting* (San Francisco), pp PP52B-03.
- 3. Wycech JB, et al. (2018) Comparison of δ18O analyses on individual planktic foraminifer (Orbulina universa) shells by SIMS and gas-source mass spectrometry. *Chem Geol* 483:119–130.
- 4. Tukey JW (1977) *Exploratory Data Analysis* (Addison-Wesley Publishing Co., Reading).
- 5. QGIS Development Team (2018) QGIS Geographic Information System.
- 6. Linzmeier BJ, Kitajima K, Denny AC, Cammack JN (2018) Making maps on a micrometer scale. *Eos (Washington DC)* 99. doi:10.1029/2018EO099269.
- 7. Bar-Matthews M, Ayalon A, Kaufman A (2000) Timing and hydrological conditions of Sapropel events in the Eastern Mediterranean, as evident from speleothems, Soreq cave, Israel. *Chem Geol* 169(1–2):145–156.
- 8. Kagan EJ (2002) Dating large earthquakes using damaged cave deposits, Soreq and Har-Tuv caves, central Israel. Geological Survey of Israel, GSI/19/2002 (Jerusalem, Israel).
- 9. Kagan EJ, Agnon A, Bar-Matthews M, Ayalon A (2005) Dating large, infrequent earthquakes by damaged cave deposits. *Geology* 33:261–264.
- 10. Bronk Ramsey C (2008) Deposition models for chronological records. *Quat Sci Rev* 27:42–60.
- 11. Kutzbach JE, Chen G, Cheng H, Edwards RL, Liu Z (2014) Potential role of winter rainfall in explaining increased moisture in the Mediterranean and Middle East during periods of maximum orbitally-forced insolation seasonality. *Clim Dyn* 42(3–4):1079–1095.
- 12. Ayalon A, Bar-Matthews M, Sass E (1998) Rainfall-recharge relationships within a karstic terrain in the Eastern Mediterranean semi-arid region, Israel: δ^{18} O and δ D characteristics. *J Hydrol* 207:18–31.
- 13. Orland IJ, et al. (2009) Climate deterioration in the Eastern Mediterranean as revealed by ion microprobe analysis of a speleothem that grew from 2.2 to 0.9 ka in Soreq Cave, Israel. *Quat Res* 71(1):27–35.
- 14. Ayalon A, Bar-Matthews M, Schilman B (2004) *Rainfall isotopic characteristics* at various sites in Israel and the relationships with unsaturated zone water. Geological Survey of Israel, GSI/16/2004 (Jerusalem, Israel).
- 15. Kaufman A, Bar-Matthews M, Ayalon A, Carmi I (2003) The vadose flow above Soreq Cave, Israel: a tritium study of the cave waters. *J Hydrol* 273(1–4):155–163.
- 16. Orland IJ, et al. (2012) Seasonal resolution of Eastern Mediterranean climate change since 34ka from a Soreq Cave speleothem. *Geochim Cosmochim Acta*

- 89:240-255.
- 17. Affek HP, Bar-Matthews M, Ayalon A, Matthews A, Eiler JM (2008) Glacial/interglacial temperature variations in Soreq cave speleothems as recorded by 'clumped isotope' thermometry. *Geochim Cosmochim Acta* 72(22):5351–5360.
- 18. Bar-Matthews M, Ayalon A, Matthews A, Sass E, Halicz L (1996) Carbon and oxygen isotope study of the active water-carbonate system in a karstic Mediterranean cave: Implications for paleoclimate research in semiarid regions. *Geochim Cosmochim Acta* 60(2):337–347.